High inductance fractal inductors for wireless applications

Akhendra Kumar PADAVALA*, Bheema Rao NISTALA
Department of Electronics and Communication Engineering, National Institute of Technology, Warangal, India

Abstract: This paper presents fractal-based inductors for industrial, scientific, and medical applications in a frequency range of 3–500 MHz. The proposed inductors are designed based on the Hilbert space-filling curve and omega-shaped space-filling curve. The fractal inductors are designed and simulated by using a full wave high frequency structural simulator. The Hilbert curve-based fractal loop inductor and omega curve-based fractal loop inductor achieve improvements in the inductance value of 21% to 31% and 11% to 30.88%, respectively, over reported standard inductors. The printed inductors are constructed on 3.2 mm RT/Duroid 5770 substrate and measured with a network analyzer (E8363B). It was found that the experimental results are almost in good agreement with the simulation results. It was also observed that the proposed fractal inductors have poor radiating power, indicating no significant electromagnetic radiation.

Key words: High frequency structural simulator, inductance value, printed circuit board, quality factor, self resonant frequency

1. Introduction

Passive components play a vital role in the overall system performance of industrial, scientific, and medical wireless communication systems. The inductor is a critical and extensively used component among all of the passive components in many circuit applications such as power amplifiers [1], matching networks [2] and DC-DC converters [3]. High inductance values (L), high quality factor (Q), and maximum achievable self resonant frequency are the three important aspects of inductor design. Obtaining larger values of inductance usually implies longer conductive segments, leading to a larger on-chip area. Inductors designed by using fractal geometry could potentially solve this problem. Fractal inductors were first reported in [4–6] but suffer from anticurrent pathways. An intuitive study of mathematically defined fractal space-filling inductors was carried out in [7–9]. The inductor designs were more competitive at lower fractal iterations but, at higher fractal iterations, the designs yield lower value of inductance compared to serpentine structures along with anticurrent pathways. The fractal loop inductors reported in [10] had higher inductance values at higher iterations. However, these designs were restricted to lower order frequencies and single layer fabrication process. In the current study, anticurrent pathways were reduced by adopting a loop structure and a multilayer fabrication process. This multilayer fabrication of the component can further increase the L.

This paper is organized as follows. Section 2 presents the constructional details of fractal inductors. Section 3 presents the simulation and experimental results, and Section 4 presents the conclusion.

---
*Correspondence: akhendra.p@gmail.com

2. Proposed fractal inductors

In general, fractal curves are characterized by two parameters, namely the iteration order (IO) and the indentation factor (IF). The proposed Hilbert fractal inductor is designed by using first order IO with indentation depth (ID) as the IF. An omega-based fractal inductor is designed by using an omega curve with the IR as '3' and the indentation angle (IA) as the IF. The proposed fractal inductors are fabricated using a RT/Duroid 5770 with a thickness of 1.6 mm, a dielectric constant of 2.33, and a loss tangent of 0.0009.

The proposed fractal inductor structure is shown in Figure 1. The corresponding equivalent circuit is shown in Figure 2. In the figure, 'R' indicates losses associated with a metal wire that is very limited for high conductivity metals. Proximity and eddy current losses associated with 'R' are also less significant at the operating frequency of 3–500 MHz. 'L' is the actual L, 'C_{int}' is the intertwining capacitance between the metal lines, and 'C_{sub}' is the capacitance between the metal lines and the substrate. The effective inductance is a combination of 'L' (inductance value) and the two parasitic capacitance values forming a frequency dependent inductor. At lower frequencies, the effect of parasitic capacitances are lower and its value increases with frequency. The variation in L with frequency is especially required for the optimal performance of circuits.
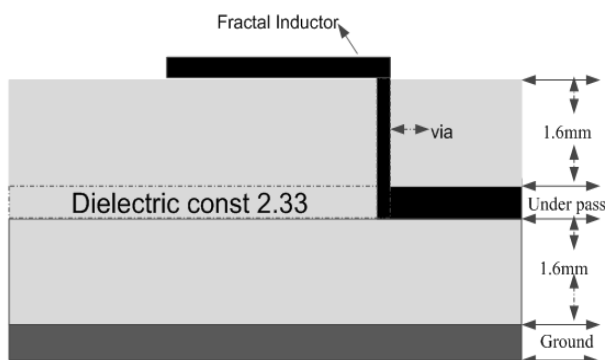

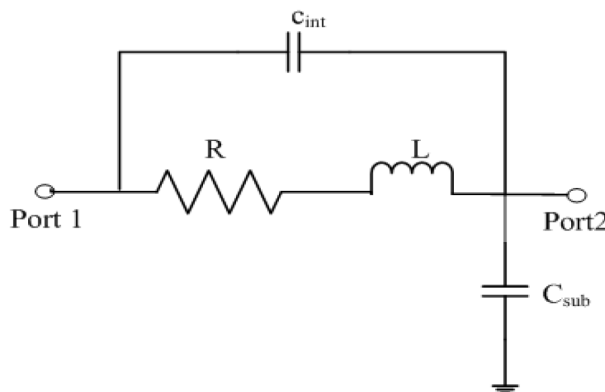Figure 1. Proposed fractal inductor structure.

Figure 2. Equivalent fractal inductor structures on PCB.

2.1. Construction of the Hilbert curve-based fractal inductor

The proposed Hilbert curve-based fractal inductor is shown in Figure 3. It was designed by using the Hilbert curve with the IO as '1' and the ID as the IF. The space-filling property of the Hilbert curve has been exploited to increase the metal run of the conductor, which leads to an increase in the L.

2.2. Construction of the omega curve-based fractal loop inductor

The proposed omega curve-based fractal loop inductor is shown in Figure 4. It was designed by using an omega curve with the IO as '3' and the IA as the IF. The L of the omega curve-based fractal loop inductor increases with the order.

2.3. Mathematical extraction of inductance

For the proposed operating range of 3–500 MHz, inductance can be extracted using analytical expressions, as reported in [11]. According to Green's function, the total inductance of the proposed inductor is the sum of the self inductance of each segment and mutual inductance between the segments [12], given by Eq. (1).

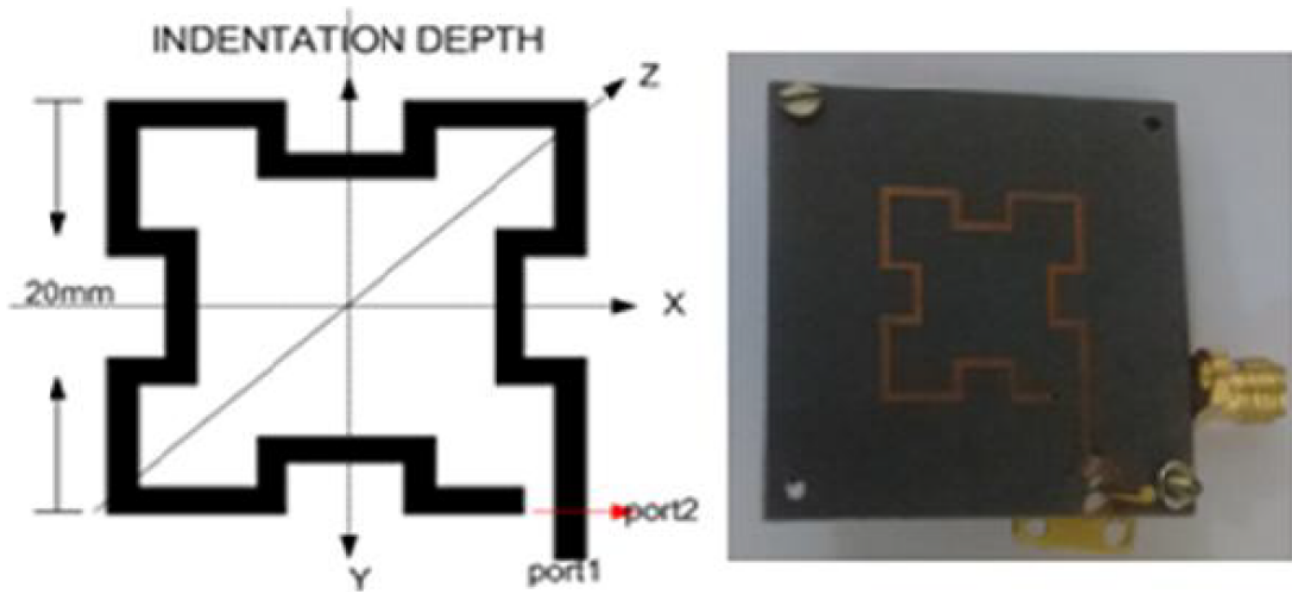$$\mathbf{L_T = L_{self} + L_m} \tag{1}$$

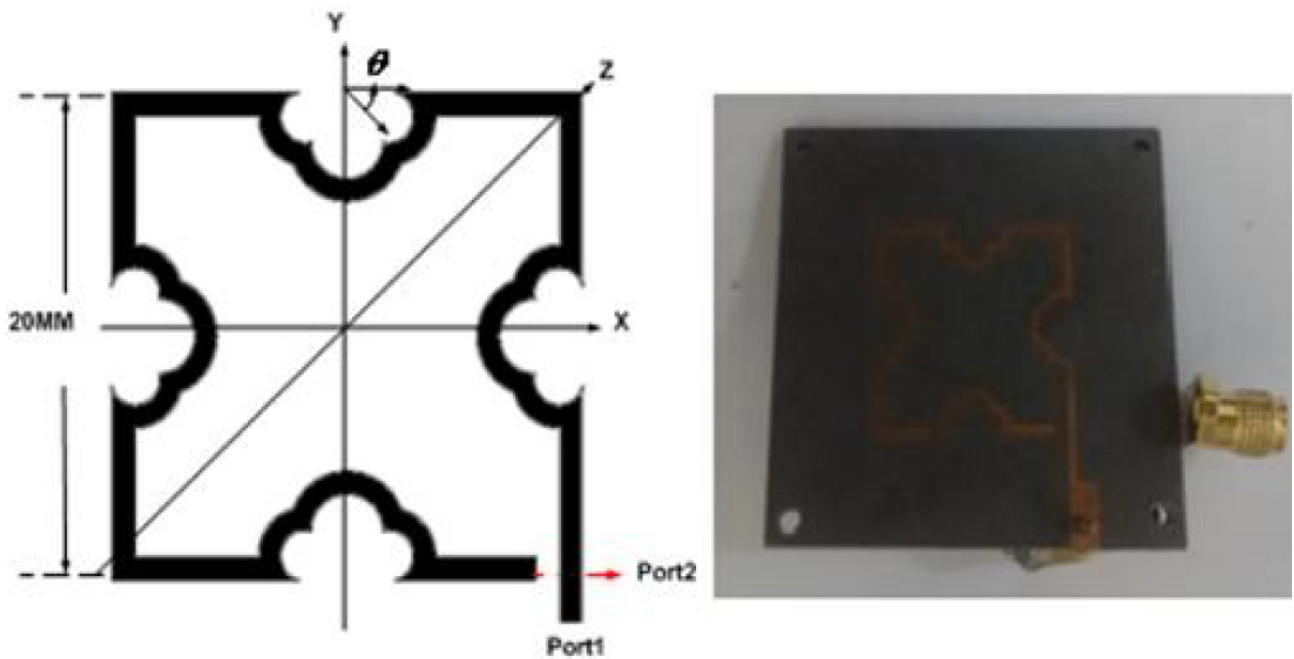**Figure 3.** Hilbert curve-based fractal loop inductor.

Figure 4. Omega curve-based fractal loop inductor.

2.3.1. Self inductance calculations

The self inductance of each segment shown in Figure 5 is calculated by axial filament approximation given by Neumann's inductance formula [13], given by Eq. (2):

$$L_{self} = \frac{1}{w^2} \int\limits_{x_2=0}^{w} \int\limits_{x_1=0}^{w} M_f dx_1 dx_2 \tag{2}$$
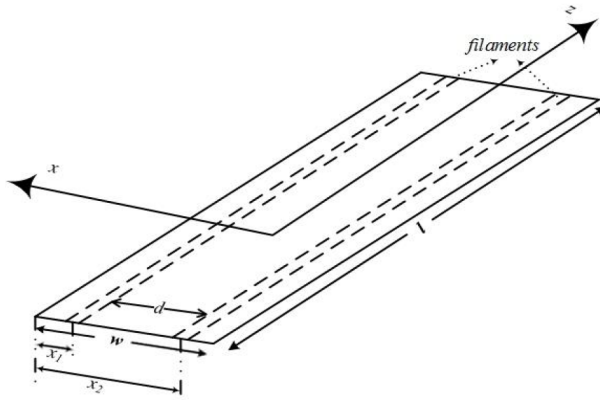
Figure 5. Trace of rectangular segment.

Here $'M_f'$ is the mutual inductance between the two assumed filaments, which are part of the segment, separated by a distance 'd' and given by Eq. (4):

$$d^2 = (x_1 - x_2)^2 \tag{3}$$

$$M_f = \frac{\mu_0}{4\pi} \left[f\left(z\right) \right] \left| \begin{array}{l} l, -l \\ (Z) \\ 0, \, 0 \end{array} \right. \tag{4}$$

Here

$$f\left(z\right) = z\,ln(z + \sqrt{z^2 + d^2}) - (\sqrt{z^2 + d^2}) \tag{5}$$

After integrating Eq. (2), the self inductance is obtained as

$$L_{self} = \frac{\mu_0}{4\pi} \frac{1}{w^2} \left[\; lw^2 ln \left(\frac{l}{w} + \sqrt{\left(\frac{l}{w}\right)^2 + 1} \right) + l^2 w \, ln \left(\frac{w}{l} + \sqrt{\left(\frac{w}{l}\right)^2 + 1} \right) \; + \ldots \right.$$

$$\ldots \frac{1}{3} \left(l^3 + w^3 \right) - \frac{1}{3} \left(l^2 + w^2 \right)^{3/2} \tag{6}$$

Similarly, the self inductance of a minor lobe, shown in Figure 6, with 'φ' being the angular limit and 'C' being the full circumference of a single loop with radius 'r', is given by Eq. (7):

$$L_{self} = N \frac{\mu_0}{2\pi} \int\limits_{\emptyset = \frac{11\pi}{18}}^{2\pi} \int\limits_{r=0}^{r - \frac{H}{2}} \frac{1}{r^2} \left[\frac{a^2 \cos\emptyset \, (a - r\cos\emptyset)}{(a^2 + r^2 - 2ar\cos\emptyset)^{3/2}} \, d\emptyset \right] r \, dr \, d\emptyset \tag{7}$$

After simplification, the self inductance of a loop is given by Eq. (8):

$$L_{self} = N \frac{\mu_0}{2\pi} \left\{ ln \left(\frac{8\pi r}{H} \right) - \frac{7}{18} \ln \left(\frac{8\pi r}{H} \right) \right\} \tag{8}$$

2.3.2. Mutual inductance calculations

For calculating the mutual inductance 'L_m' between the conductor segments of an inductor, there are four possible configurations for any two segments of fractal inductors: (i) the segments that are offset are
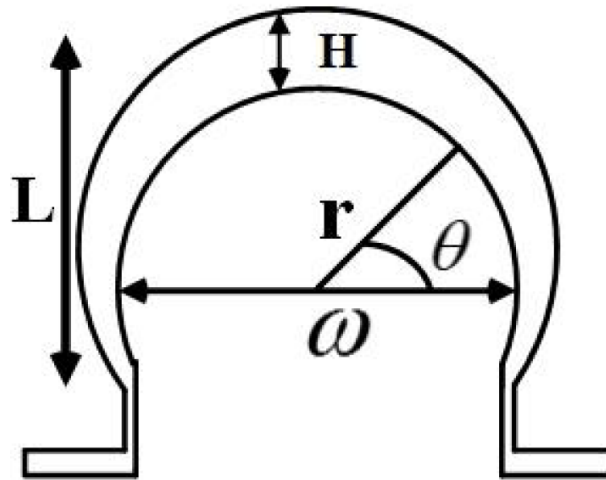
Figure 6. Trace of minor lobe with radius.

parallel, (ii) the segments are aligned, (iii) the segments are parallel, and (iv) the filaments are perpendicular. In the last case, partial mutual inductance between any two perpendicular filaments is always zero.

Considering case (i), the segments that are offset are parallel, as shown in Figure 7a. Mutual inductance between the two filaments is given as
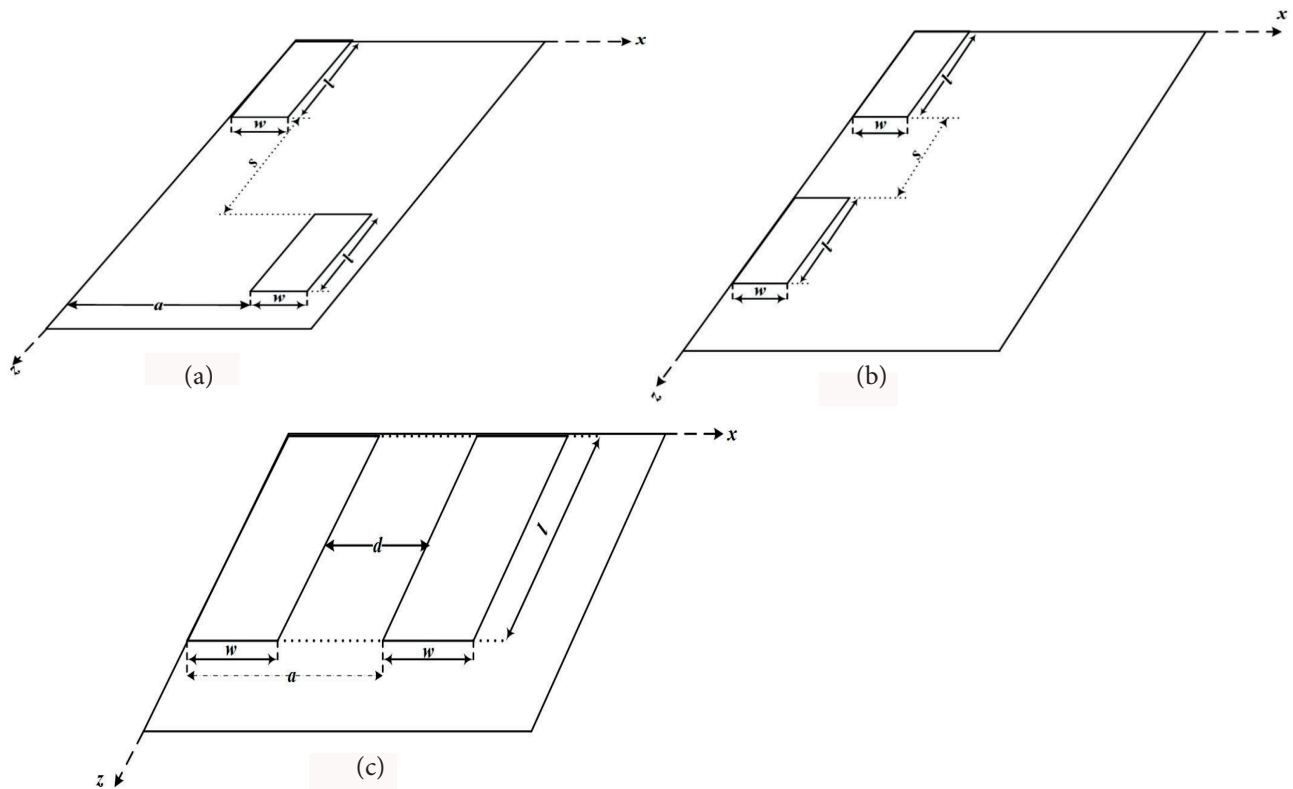

Figure 7. Mutual inductance between a pair of segments: a) mutual inductance between a pair of segments that are offset, b) mutual inductance between a pair of segments that are aligned, c) mutual inductance between two segments.

$$M_f = \frac{\mu_0}{4\pi}[f(z)] \begin{vmatrix} (l+s+m),\, s \\ (z) \\ (s+m),\, (l+s) \end{vmatrix}, \tag{9}$$

where

$$f(z) = zln(z + \sqrt{z^2 + d^2}) - (\sqrt{z^2 + d^2}) \tag{10}$$

$$d^2 = (x_1 - x_2)^2 \tag{11}$$

Mutual inductance is given by Eq. (12):

$$L_m = \frac{1}{w^2} \int\limits_{x_2=0}^{a+w} \int\limits_{x_1=0}^{w} M_f \, dx_1 \, dx_2 \tag{12}$$

After solving the above equation, 'L_m' is obtained as s

$$L_m = \frac{\mu_0}{4\pi} \frac{1}{w^2}[f(x,\,z)] \begin{vmatrix} (a+w),\, (a-w) \\ (x) \\ (a),\, (a) \end{vmatrix} \begin{vmatrix} (l+m+s),\, s \\ (z) \\ (s+m),\, (l+s) \end{vmatrix} \tag{13}$$

In case (ii), the segments are aligned, as shown in Figure 7b. This is obtained by replacing '$a = 0$' in Eq. (13):

$$L_m = \frac{\mu_0}{4\pi} \frac{1}{w^2}[f(x,\,z)] \begin{vmatrix} w,\, -w \\ (x) \\ 0,\, 0 \end{vmatrix} \begin{vmatrix} (l+m+s),\, s \\ (z) \\ (s+m),\, (l+s) \end{vmatrix} \tag{14}$$

In case (iii), the segments are parallel, as shown in Figure 7c. This is obtained by replacing '$s = -l$', '$l = m$' in Eq. (13):

$$L_m = \frac{\mu_0}{4\pi} \frac{1}{w^2}[f(x,\,z)] \begin{vmatrix} (a+w),\, (a-w) \\ (x) \\ a,\, a \end{vmatrix} \begin{vmatrix} l,\, -l \\ (z) \\ 0,\, 0 \end{vmatrix}, \tag{15}$$

where

$$f(x,\,z) = \frac{x^2}{2} z \, ln\left(z + \sqrt{z^2 + x^2}\right) - \frac{1}{6}\left(z^2 + x^2\right)\sqrt{z^2 + x^2}\,... \tag{16}$$

$$.... + \frac{z^2}{2} x \, ln\left(x + \sqrt{z^2 + x^2}\right)$$

Mutual inductance between adjacent lobes at an angle to each other, as shown in Figure 8, is given by Eq. (17):

$$L_m = \frac{\mu_r \mu_0}{4\pi} \cos\theta_n \int_l {}_n \int_{m_n},\, \frac{1}{P_n} \, dl_n \, dm_n \tag{17}$$

Eq. (17) can be simplified as

$$L_m = \frac{\mu_r \mu_0}{4\pi} \cos\theta_n \left[l_n \, ln\frac{P_n + m_n + l_n}{P_n + l_n - m_n} + m_n \, ln\frac{P_n + m_n + l_n}{P_n + l_n - m_n} \right] \tag{18}$$
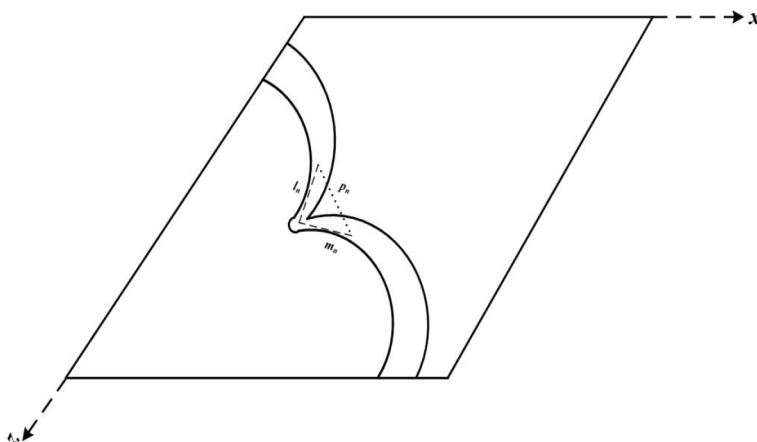
Figure 8. Mutual inductance between lobes.

For a fractal '$l = m$'

$$L_m = \frac{\mu_0}{4\pi} \cos\theta_n \, 2l_n \left(\ln \frac{P_n + 2l_n}{P_n} \right) \tag{19}$$

2.4. Radiation from the PCB inductor

The electromagnetic radiation of the PCB inductor reported theoretically in [14] shows that far-field radiation is negligible for HF applications. The radiated power of the proposed inductors is given by Eq. (20):

$$P = \frac{160 \, \pi^4 I^2 a^4 f_c^4}{c^4}, \tag{20}$$

where 'I' is the current in the loop, 'a' is the side of the loop, ''f_c' is the operating frequency, and 'c' is the speed of light.

The maximum radiated power of the proposed inductors, with sides of 20 mm, are almost negligible within a frequency range of 3–500 MHz. Corresponding radiation plots are shown in Figure 9.

2.5. Comparison of the printed circuit board inductor with a silicon inductor

The inductor is usually fabricated either on a printed circuit board (PCB) or on silicon. Inductors fabricated on silicon suffer from a low Q with high fabrication cost. Extra processing steps such as etching and micromachining are required to increase the Q of the silicon inductor. Moreover, the Q obtained will not be more than 25. Low temperature cofired ceramic is another process used to fabricate inductors that provides a high L, but it requires a ferrite core that reduces the self-resonant frequency. Inductors fabricated on a standard PCB have higher inductance and Q. A summary of the comparison between silicon and PCB inductors is provided in the Table.

3. Results and discussion

3.1. Simulation results

The design, modeling, and simulation of the proposed fractal inductors were performed and analyzed using a finite electromagnetic simulator HFSS provided by the Ansys Corporation. The proposed fractal inductors are compared with meander and standard 2nd order Hilbert fractal inductors with similar substrates, layout sizes, and operating frequencies. The layouts of the meander and standard 2nd order Hilbert fractal inductors are
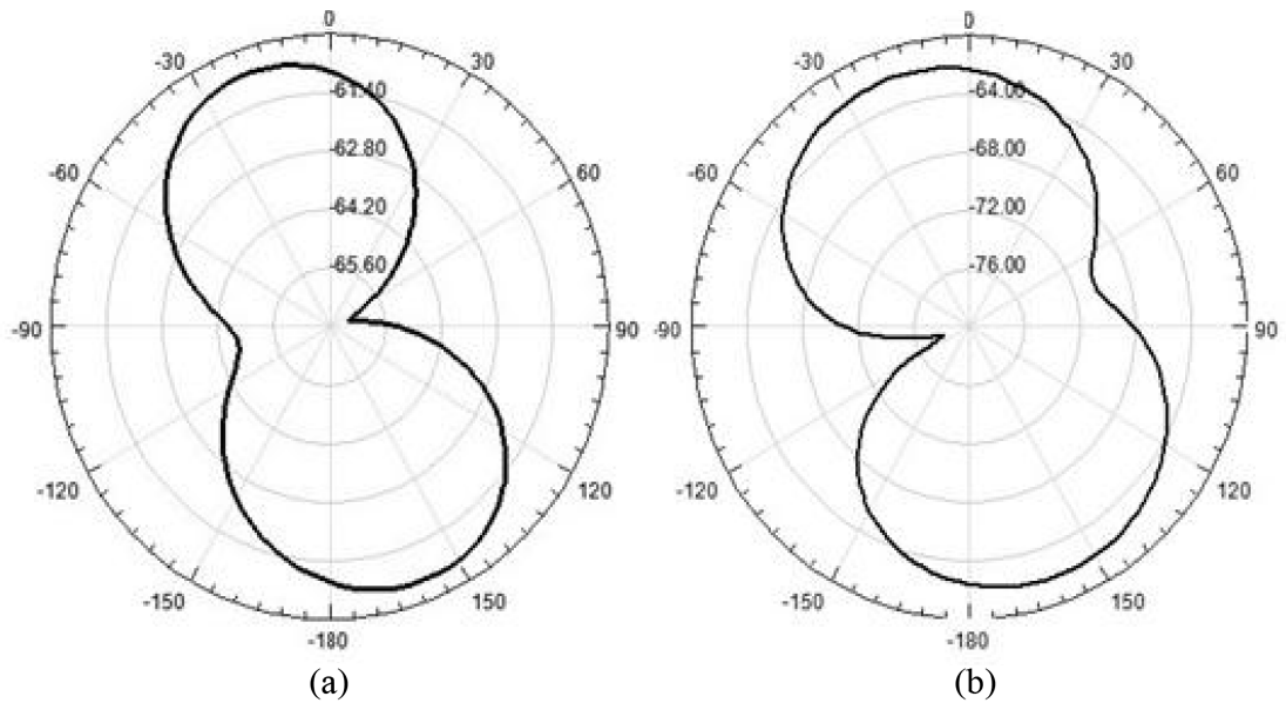
Figure 9. Radiation pattern measure: a) Hilbert-based fractal loop inductor, b) omega-based fractal loop inductor.

Table. Comparison between the silicon inductor and PCB inductor.

Trade offs	Silicon substrate	RT/Duroid substrate
Cost	Thousands of $	Hundreds of $
Fabrication complexity	Processing steps are more	Processing steps are less
Frequency range	GHz	MHz
Inductance	nH	mH
Q-factor	< 20	> 50

shown in Figure 10. From the simulation results shown in Figure 11, it can be observed that the proposed Hilbert curve-based fractal loop inductor has an inductance that is 21% greater than that of the 2nd iterative Hilbert fractal inductor and 31% greater than that of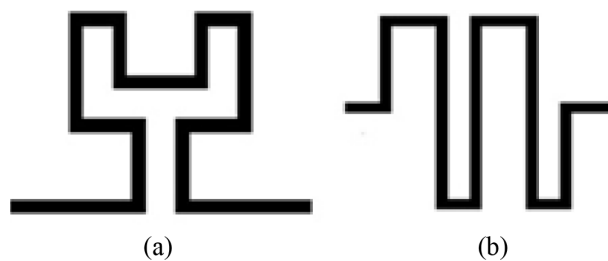 the meander inductor, respectively. In addition, from the simulation results shown in Figure 12, the proposed omega-based fractal loop inductor has an inductance that is 11% greater than that of the 2nd iterative Hilbert fractal inductor and 31% greater than that of the meander inductor, respectively.

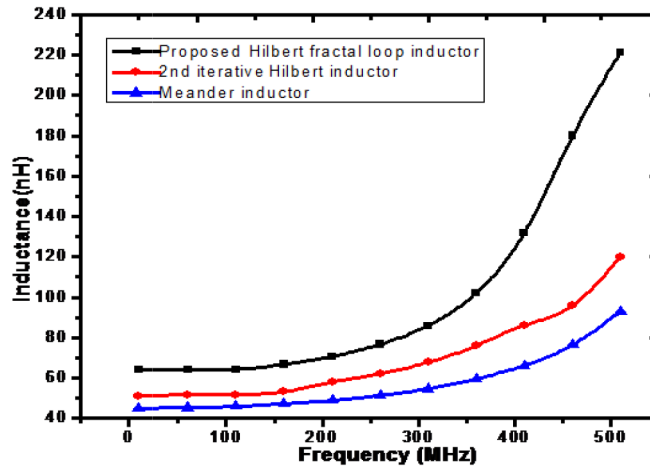**Figure 10.** Layout of different standard fractal inductors: a) Hilbert curve-based inductor, b) meander inductor.

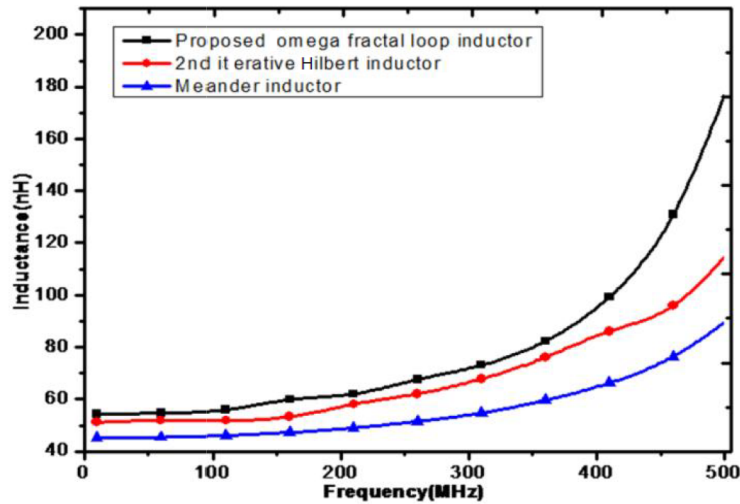**Figure 11.** Comparison of Hilbert-based fractal loop inductor inductance values with various standard inductors.

Figure 12. Comparison of omega curve-based loop inductor inductance values with various standard inductors.

3.2. Experimental results

The proposed inductors are fabricated on a PCB with an outer diameter of 20×20 mm^2. The fractal inductor and the ground plane are separated by a dielectric at a thickness of 3.2 mm, and the return path and the ground plane are separated by 1.6 mm. The internal turn and the return path are connected by a via. Experimentation is carried out on the fabricated inductor using a network analyzer (E8363B) that was calibrated with the short-open-load-through calibration technique. The measurement setup is shown in Figure 13. The L and Q are calculated from Y parameters obtained from S parameters using the following equations:

$$Y_{11} = \frac{(1 - S_{11}) * (1 + S_{22}) + S_{12} * S_{21}}{(1 + S_{11}) * (1 + S_{22}) - S_{12} * S_{21}} \tag{21}$$

$$Y_{12} = \frac{-2 * S_{12}}{(1 + S_{11}) * (1 + S_{22}) - S_{12} * S_{21}} \tag{22}$$
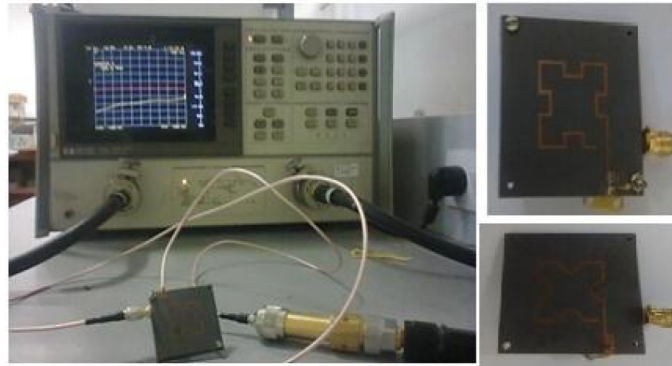
Figure 13. Set up for measuring the fractal inductors.

$$Y_{21} = \frac{-2 * S_{21}}{(1 + S_{11}) * (1 + S_{22}) - S_{12} * S_{21}} \tag{23}$$

$$Y_{22} = \frac{(1 + S_{11}) * (1 - S_{22}) + S_{12} * S_{21}}{(1 + S_{11}) * (1 + S_{22}) - S_{12} * S_{21}} \tag{24}$$

$$Inductance\,(L) = \frac{-1}{(2\pi f * Im\,(Y_{11}))} \tag{25}$$

$$Q\,factor = \frac{-Im(Y_{11})}{Re(Y_{11})} \tag{26}$$

The experimental and simulation results of the Hilbert fractal loop inductor in terms of S parameters (S_{11} & S_{21}) are shown in Figure 14. From the results, the value of the magnitude of S_{21} decreases with an increase in
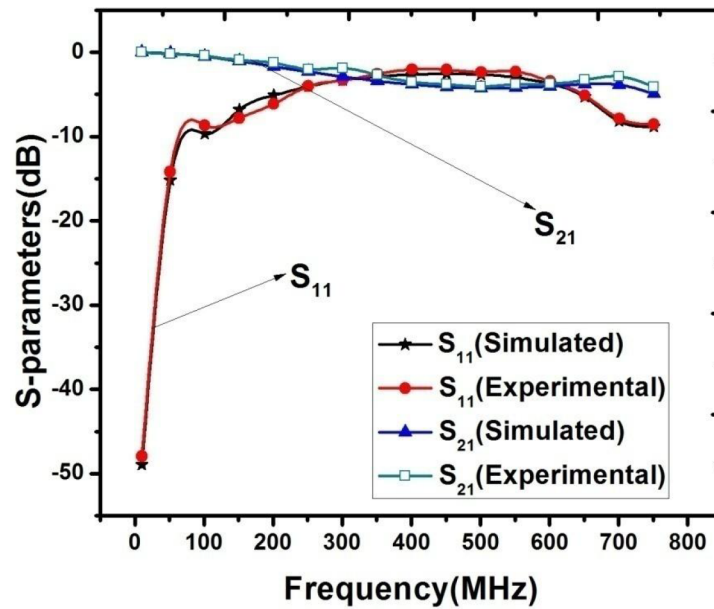

Figure 14. Measurement and simulation: S parameter results of the Hilbert curve-based fractal loop inductor.

frequency until it attains a minimum value at a frequency known as the self-resonant frequency of the inductor. Similarly the magnitude of S_{11} is minimum at lower frequencies, and its value increases with an increase in frequency. The variation in the values of S_{21} & S_{11} is due to the increase in parasitic capacitances of the substrate and the coil. The corresponding Ls are derived from the S parameters, as shown in Figure 15. From the results, it can be observed that the L increases with frequency.
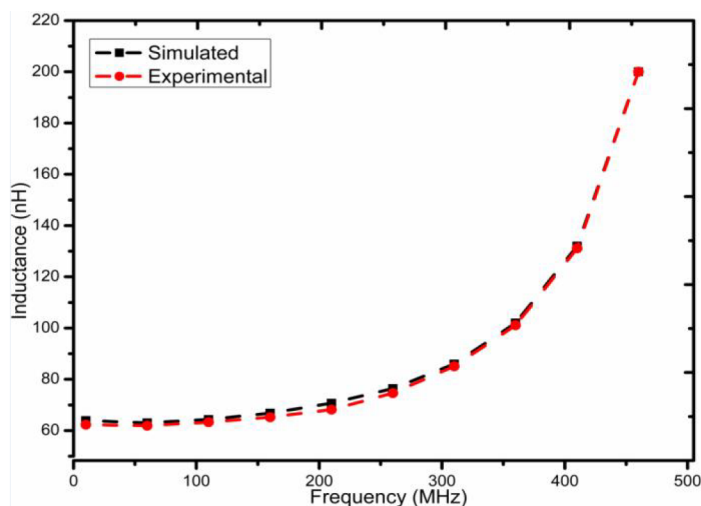

Figure 15. Measurement and simulation: inductance results of the Hilbert curve-based fractal loop inductor.

The experimental and simulation results of the omega-based fractal loop inductor in terms of S parameters (S_{11} & S_{21}) are shown in Figure 16. From the results, it can be observed that the magnitude of S_{21} decreases with an increase in frequency until it attains a minimum value at a frequency known as the self-resonant frequency of the inductor. Similarly, the magnitude of S_{11} is minimum at lower frequencies, and its value increases with an increase in frequency. The variation of S_{21} & S_{11} is due to the increase in parasitic capacitances of the substrate and the coil. The corresponding Ls are derived from the S parameters, as shown in Figure 17.
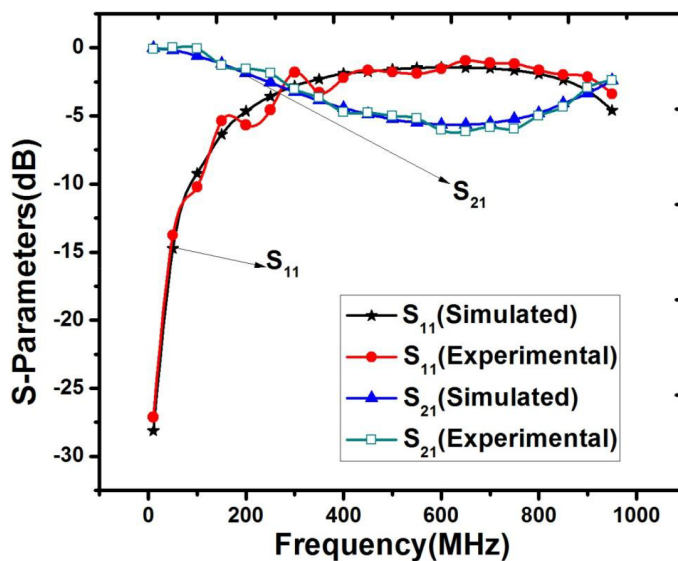

Figure 16. Measurement and simulation: S parameter results of the omega-based curve fractal loop inductor.
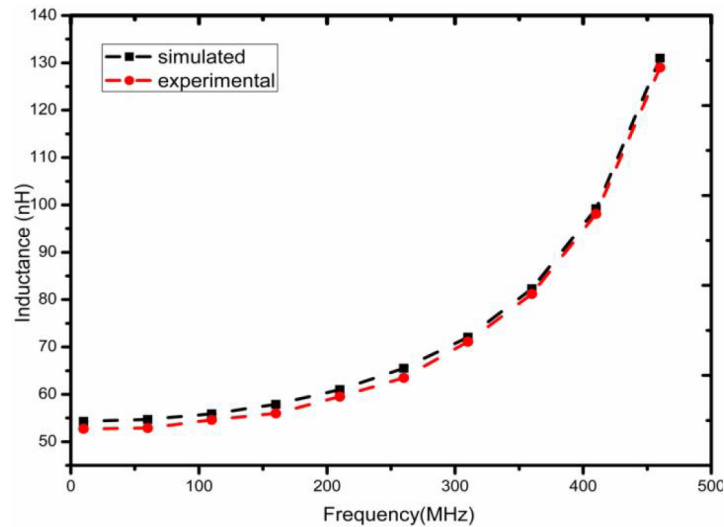
Figure 17. Measurement and simulation results of the omega-based curve fractal loop inductor.

From the results, it can be observed that the L increases with frequency. The results show that the experimental results are in good agreement with the simulation results.

4. Conclusion

Inductors designed based on the Hilbert space-filling curve and omega shaped space-filling curve have been proposed. The results show that the proposed fractal inductors have a higher L with a moderate Q value over standard reported inductors. The proposed inductors are suitable for wireless applications in a frequency range of 3–500 MHz. Moreover, the radiated power of the proposed inductors is much lower so that it acts as an inductor rather than a radiating element in a frequency range of 3–500 MHz.

References

[1] Yang JR, Son HC, Park YJ. A class E power amplifier with coupling coils for a wireless power transfer system. Prog Electromagn Res 2013; 3: 13-22.

[2] Chung J, Hamedi-Hagh S. Design of PCB impedance matching inductors and antennas for single-chip communication systems. International Journal of Microwave Science and Technology 2008; 2008: 1-7.

[3] Orlandi S, Allongue B, Blanchot G, Buso S, Faccio F, Fuentes C, Kayal M, Michelis S, Spiazzi G. Optimization of shielded PCB air-core toroids for high-efficiency DC–DC converters. IEEE T Power Electr 2011; 26: 1837-1846.

[4] Ho KMJ, Ellis GA, Ooi BL, Leong MS. Modeling of a coplanar waveguide meander-line inductors. Int J Rf Micro C E 2002; 12: 520-529.

[5] Stojanovica G, Damnjanovic M, Desnica V, Zivanov L, Raghavendra R, Bellew P, Mcloughlin N. High performance zig-zag and meander inductors embedded in ferrite material. J Magn Magn Mater 2006; 29: 76-83.

[6] Menicanin AB, Zivanov LD, Damnjanovic DZ, Maric AM. Low-cost CPW meander inductors utilizing ink-jet printing on ?exible substrate for high-frequency applications. IEEE T Electron Dev 2013; 60: 827-832.

[7] Wang G, Xu L, Wang T. A novel MEMS fractal inductor based on Hilbert curve. In: Computational Intelligence and Communication Networks Conference; 3–5 November 2012; Mathura, India: IEEE. pp. 241-244.

[8] Maric A, Radosavljwevic G, Zivanov M, Zivanov LJ, Stojanovic G, Mayer M, Jachimawicz A, Keplinger F. Modelling and characterization of fractal based RF inductors on silicon substrate. In: Advanced Semiconductor Devices and Microsystems Conference; 12–16 Oct 2008; Smolenice, Slovakia: IEEE. pp. 191-194.

[9] Lazarus N, Meyer CD, Bedair SS. Fractal inductors. IEEE T Magn 2014; 50:1-8.

[10] Shoute G, Barlage DW. Fractal loop inductors. IEEE T Magn 2015; 51: 1-8.

[11] Grover FW. Inductance Calculations. New York, NY, USA: Dover, 2009.

[12] Greenhouse HM. Design of planar rectangular microelectronic inductors. IEEE T Parts Hyb Pac 1974; 10: 101-109.

[13] Paul CR. Inductance: Loop and Partial. Hoboken, NJ, USA: Wiley-IEEE Press, 2010.

[14] Hui D, Yisheng Z, Baishan Z. Research on the Electromagnetic Radiation of a PCB Planar Inductor. In: Asia-Pacific Microwave Conference; 4–7 December 2005; Suzhou, China: IEEE. pp. 1-4.